COMMUNICATION

Check for updates

A transferrin-targeted nanoplatform for MRI-guided visualization and potent suppression of tumors and pulmonary metastatic lesions†

Liya Tian,‡[ab] Pengju Ma,‡[c] Wenxiu Zhuang,[c] Yinlong Xu,[d] Lihua Pang,[c] Kai Guo,[b] Ke Ren,[b] Xueli Xu,[c] Xiao Sun [ID] *[a] and Shunzhen Zheng*[d]

While targeted theranostics for cancer remains a pivotal research frontier, conventional ligand conjugation strategies exhibit persistent limitations in off-target accumulation and suboptimal tumor specificity, ultimately failing to achieve reliable detection of early-stage lesions or metastatic nodules while demonstrating insufficient therapeutic payload delivery. In this study, the manganese sulfide (MnS) nanoplatform was synthesized using transferrin (Tf) with tumor-targeting properties as a carrier by a simple fabrication method. Notably, compar'ed to clinically prevalent Gd-based contrast agents, Tf–MnS exhibited superior T_1-weighted magnetic resonance imaging (MRI) contrast performance, with the longitudinal relaxation (r_1) reaching 7.5253 mM^{-1} s^{-1}, which was significantly higher than 3.2915 mM^{-1} s^{-1} of Gd-DTPA, and in the MRI of subcutaneous tumors and lung metastatic lesions in mice, the maximum relative signal-to-noise ratios reached 46.33% and 40.33%, respectively. Remarkably, upon reaching the acidic tumor microenvironment, Tf–MnS disintegrated to release Mn^{2+} ions and hydrogen sulfide (H$_2$S). The Mn^{2+} ions participated in Fenton-like reactions to produce cytotoxic hydroxyl radicals, while H$_2$S concurrently inhibited catalase enzyme activity, thereby alleviating the insufficiency of the hydrogen peroxide substrate and amplifying the therapeutic outcome. This synergistic mechanism endowed Tf–MnS with a self-enhanced anti-tumor effect, inhibiting both lung metastatic lesions and subcutaneous tumors in mice of the Tf–MnS group, with a tumor inhibition rate of 54.26%. Collectively, this work proposes an innovative strategy for integrating accurate diagnosis and self-augmented therapy of tumors and lung metastatic lesions into a unified nanoplatform, offering a promising methodology for precision oncology.

New concepts

Conventional magnetic resonance imaging (MRI) contrast agents are limited by nonspecific systemic distribution and low tumor targeting efficiency, resulting in insufficient diagnostic sensitivity for early-stage or metastatic tumors. Although surface engineering of nanoplatforms with ligands enables active tumor targeting, the functionalization of nanomaterial surfaces with targeting ligands often faces challenges such as low conjugation efficiency. Therefore, this study employed a facile synthesis strategy using transferrin (Tf) as a template to construct a manganese sulfide (MnS) nanoplatform. This templated approach confers significantly higher ligand density, enhancing targeting capability and promoting effective accumulation at both primary tumor sites and pulmonary metastases. Meanwhile, the nanoplatform effectively decomposes within the acidic tumor microenvironment, facilitating precise diagnosis of tumors and pulmonary metastases based on MRI, and it exhibits the effect of inhibiting tumors and pulmonary metastases.

1. Introduction

Cancer poses a serious threat to public health, underscoring the imperative for accurate diagnosis and effective treatment to halt the progression of tumors. Magnetic resonance imaging (MRI) is a well-established medical imaging technology featuring multi-parametric, multi-perspective, and high soft tissue contrast imaging.[1] It has become one of the most comprehensive and effective non-invasive diagnostic and monitoring tools in the preliminary diagnosis and therapeutic evaluation of various tumor diseases.[2–4] Additionally, MRI often requires

[a] Shandong Cancer Hospital and Institute, Shandong First Medical University & Shandong Academy of Medical Sciences, Jinan 250000, China.
  E-mail: sunxiao@sdfmu.edu.cn

[b] School of Chemistry and Pharmaceutical Engineering, Medical Science and Technology Innovation Center, Shandong First Medical University and
  Shandong Academy of Medical Sciences, Jinan 250000, China

[c] School of Science, Shandong Jianzhu University, Jinan 250101, China

[d] Department of Hepatobiliary Surgery, Shandong Provincial Hospital Affiliated to Shandong First Medical University, Jinan 250021, China.
  E-mail: zsz5512920@hotmail.com

† Electronic supplementary information (ESI) available. See DOI: https://doi.org/10.1039/d5nh00325c

‡ These authors contributed equally to this work.

the assistance of contrast agents in most cases. Currently, common T_1 contrast agents include gadolinium-based and manganese-based compounds,[5–8] which can produce a significant contrast effect by altering the relaxation time of protons in water molecules under an external magnetic field. However, conventional gadolinium-based MRI contrast agents are fundamentally constrained by a nonspecific systemic biodistribution and suboptimal tumor targeting efficiency, particularly manifesting in inadequate diagnostic sensitivity for early-stage malignancies such as pulmonary nodules and micrometastatic lesions.[9] Moreover, systemic chemotherapy often suffers from off-target toxicity and insufficient drug accumulation at tumor sites.[10] These persistent challenges underscore the imperative for developing advanced targeting strategies to achieve breakthrough improvements in early-stage detection and precision oncology interventions.

The advancement of nanotechnology has revolutionized early tumor-targeted diagnosis and therapy, offering unprecedented opportunities for precision oncology.[11–13] Current research has demonstrated the efficacy of surface-engineered nanoplatforms functionalized with ligands such as programmed cell death ligand 1 antibodies and RGD (Arg-Gly-Asp) peptides, which enable active tumor targeting *via* binding to overexpressed receptors on cancer cells.[14,15] Among these strategies, transferrin (Tf), an iron-transport protein, stands out as a particularly promising targeting moiety. Notably, over 98%
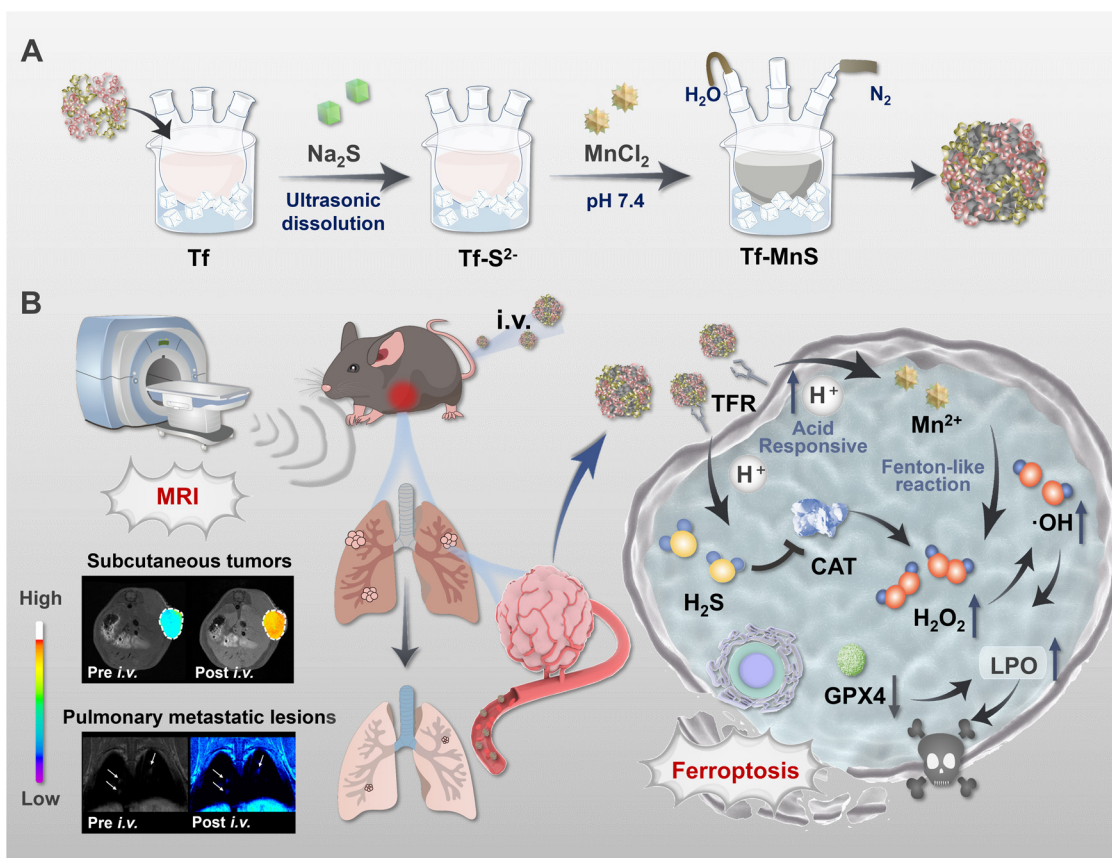
of primary and metastatic tumors exhibit upregulated expression of transferrin receptors (TfRs).[16,17] Hence, Tf not only provides efficient iron delivery but also realizes tumor-specific targeting and promotes drug accumulation in tumor cells; it has successfully enabled the effective loading of various drug molecules, imaging agents, and metal nanoparticles.[18,19] However, surface functionalization of nanomaterials with targeting ligands often faces challenges such as suboptimal conjugation efficiency and compromised targeting efficacy.

Therefore, based on Tf as a carrier, a manganese sulfide nanoplatform (Tf–MnS) was synthesized by a simple method using manganese chloride ($MnCl_2$) and sodium sulfide (Na_2S) in this study (Scheme 1A). The decomposition of MnS in an acidic environment was used to increase reactive oxygen species (ROS) levels autonomously, thereby effectively inducing tumor ferroptosis and inhibiting lung metastatic lesions. Concurrently, the released Mn^{2+} can achieve a superior T_1 MRI effect, culminating in the achievement of an MRI-guided integrative diagnostic and therapeutic approach (Scheme 1B).

2. Results and discussion

2.1 Synthesis and characterization of Tf–MnS

The synthesis of the Tf–MnS nanoplatform was systematically conducted through a three-step procedure. Initially, Tf was

Scheme 1 (A) Process of the construction of Tf–MnS. (B) Schematic illustration of Tf–MnS used for tumor diagnosis and therapy.

dissolved in a Na_2S aqueous solution, followed by pH adjustment to ~ 7.6. Subsequently, a stoichiometric amount of $MnCl_2$ aqueous solution was introduced dropwise into the mixture. The reaction system was maintained in an ice-water bath under nitrogen atmosphere protection, with vigorous stirring sustained for 4 h to ensure complete nanoparticle formation.

The characterization process was crucial to verify the structure and elemental composition of the Tf–MnS nanoplatform. Transmission electron microscopy (TEM) analysis revealed that Tf–MnS exhibited a uniform size and excellent dispersion (Fig. 1A and B), and TEM mapping elemental analysis confirmed the composition of Tf–MnS, which includes C, O, N, Fe, Mn and S elements (Fig. 1C). Additionally, Tf–MnS with an
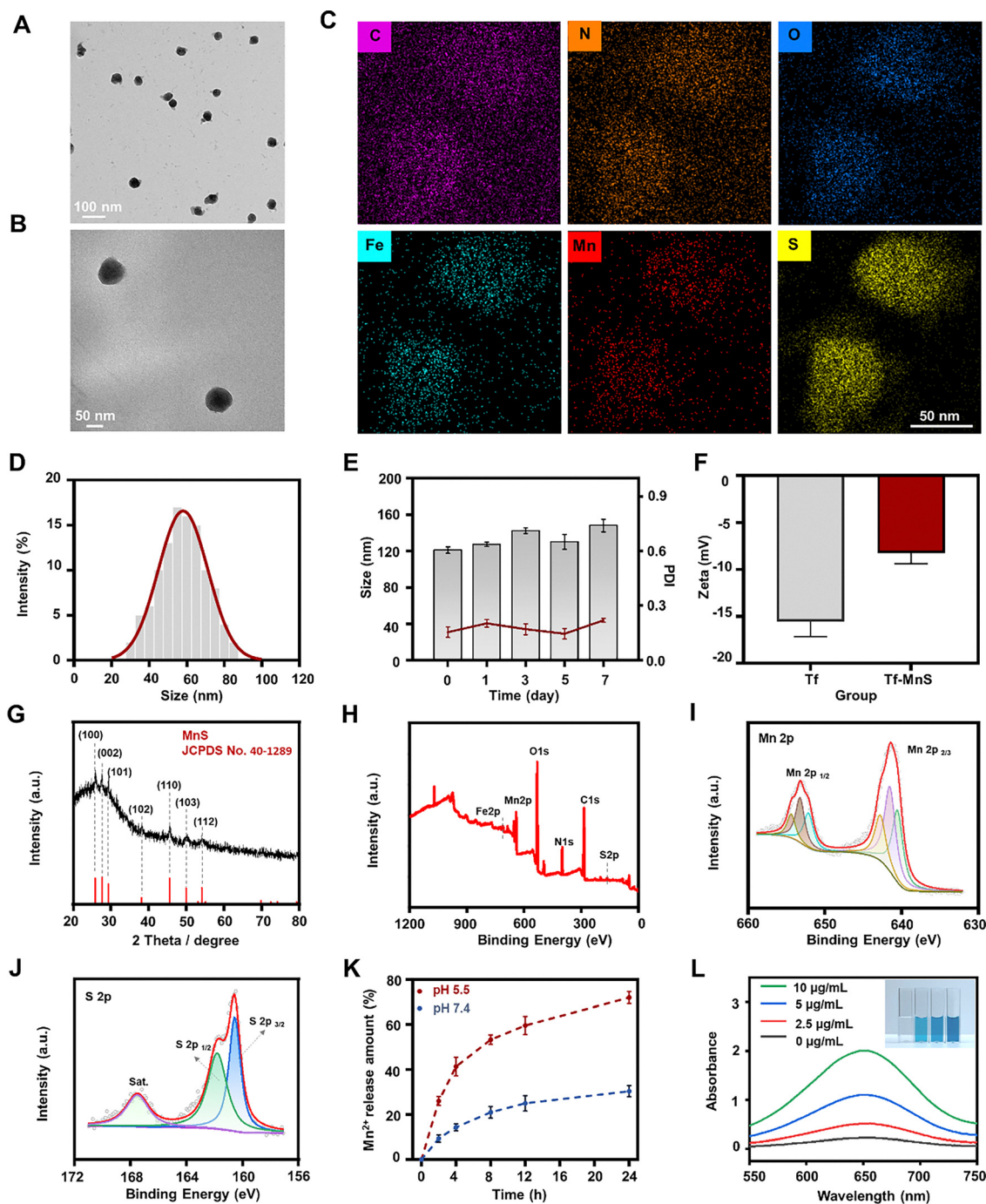

Fig. 1 (A) and (B) TEM images of Tf–MnS. (C) Elemental mapping analysis of Tf–MnS. (D) Particle size distribution of Tf–MnS. (E) Stability evaluation of Tf–MnS in DMEM containing 10% FBS ($n = 3$). (F) Zeta potential analysis of Tf and Tf–MnS. (G) XRD patterns of Tf–MnS. (H) XPS spectra of Tf–MnS, (I) for the Mn 2p regions and (J) S 2p regions. (K) Release of Mn^{2+} under different pH conditions. (L) TMB color changes of the H_2O_2 solution with Tf–MnS treatment and the corresponding UV absorption.

average particle size of approximately 58.01 $\pm$ 13.17 nm (Fig. 1D), and the stability of Tf–MnS was assessed in DMEM containing 10% FBS. The polydispersity index (PDI) within seven days was all less than 0.3 (Fig. 1E), indicating that Tf–MnS has good dispersion and stability. Due to the abundance of amino groups in MnS, Tf–MnS displayed a slightly less negative charge of about -8.24 ± 1.16 mV compared to the -15.51 ± 1.65 mV zeta potential of Tf (Fig. 1F), indicating successful synthesis of the Tf–MnS nanoplatform. The X-ray diffraction (XRD) analysis demonstrated that distinct diffraction peaks correspond to the spinel structure of MnS, aligning with the MnS standard card (PDF#40-1289) (Fig. 1G). The X-ray photoelectron spectroscopy (XPS) survey scan of the Tf–MnS nanoplatform confirmed the presence of C, N, O, Fe, Mn, and S elements (Fig. 1H). In the Mn 2p XPS spectrum, two distinct peaks centered at 653.18 eV and 641.48 eV were assigned to Mn $2p_{1/2}$ and Mn $2p_{3/2}$, respectively (Fig. 1I). Furthermore, the S 2p spectrum exhibited two characteristic peaks at 161.68 eV and 160.58 eV, corresponding to the S $2p_{1/2}$ and S $2p_{3/2}$ orbitals (Fig. 1J). Additionally, in the Fe 2p XPS spectrum, two prominent peaks located at 723.88 eV and 710.58 eV were identified, corresponding to Fe $2p_{1/2}$ and Fe $2p_{3/2}$ orbitals, respectively (Fig. S1, ESI†). Next, the properties of the materials were investigated. The release of Mn^{2+} was relatively low at pH 7.4 but increased significantly at pH 5.5, confirming the pH-responsiveness of Tf–MnS (Fig. 1K). Tetramethylbenzidine (TMB) assay results showed that Tf–MnS can catalyze hydrogen peroxide (H_2O_2) to generate amounts of $^{\bullet}OH$ in a dose-dependent manner. The H_2S-generating capacity of Tf–MnS under different pH conditions was evaluated using the silver nitrate assay. The results demonstrated significantly enhanced silver sulfide precipitation formation at pH 5.5 compared to pH 7.4 (Fig. S2, ESI†), indicating pH-dependent H_2S release with superior production under acidic conditions. In conclusion, the experimental results of material characterization and properties show that the Tf–MnS nanoplatform has been successfully synthesized, and it has been confirmed that it is pH responsive, highlighting its potential for future applications in MRI-guided cancer diagnosis and treatment.

2.2 Characterization of the biological properties of Tf–MnS

Next, the *in vitro* uptake ability of Tf–MnS was verified by various experiments. Confocal laser scanning microscopy (CLSM) was used for observing the distribution of Tf–MnS in mouse Lewis lung cancer (LLC) cells after co-incubation for 4 h (Fig. 2A and Fig. S3, ESI†). The figures showed that the Cy5.5 red fluorescence was predominantly observed in the cytoplasm, but prior incubation of LLC cells with excess free Tf resulted in a decrease in the intracellular Tf–MnS-Cy5.5 fluorescence intensity, unequivocally validating the targeted uptake of the Tf-mediated nanoplatform. Additionally, the uptake of Tf–MnS in LLC cells and other normal cells, such as mouse embryonic fibroblast cells (NIH/3T3), human umbilical vein endothelial cells (HUVEC) and mouse lung epithelial cells (MLE-12), was observed using CLSM. The results indicated that the red fluorescence in LLC cells was significantly higher than that in

the other three normal cell lines (Fig. S4, ESI†), and it indicates that Tf–MnS has a good targeting effect on LLC cells. Then the internalization mechanism of Tf–MnS was investigated as follows. The CLSM images of cells treated with various endocytosis inhibitors demonstrated that the red fluorescence intensity decreased significantly after low temperature treatment at 4 °C and methyl-β-cyclodextrin (M-β-CD, an inhibitor of caveolin mediated endocytosis) in both groups, indicating that the uptake of Tf–MnS was inhibited. However, the fluorescence intensity of the two groups treated with chlorpromazine (CPZ, inhibitor of clathrin mediated endocytosis) and amiloride (inhibitor of macropinocytosis) treatment did not show significant changes compared with the Tf–MnS group. The pictures taken by CLSM and the corresponding quantitative analysis directly indicate that the pathway of Tf–MnS into cells is mainly caveolin mediated endocytosis and is energy dependent. Next, analysis using flow cytometry (FCM) and inductively coupled plasma optical emission spectrometry (ICP-OES) for analysis of the Mn^{2+} content also demonstrated the effective internalization of Tf–MnS in LLC cells in a dose- and time-dependent manner (Fig. 2B and C). Furthermore, molecular docking analysis validated the strong binding affinity between Tf and TfRs overexpressed on tumor surfaces, which substantiates the tumor-targeted delivery mechanism of Tf–MnS (Fig. 2D).

Subsequently, the cytotoxicity of the Tf–MnS nanoplatform was verified. The findings revealed a gradual decrease in cell survival rates with increasing Mn^{2+} concentrations. The results of the MTT experiment show that the survival rate of MLE cells and HUVEC remained above 80% even at a concentration of 80 μg mL^{-1} (Fig. S5, ESI†), while the survival rate of LLC cells dropped significantly to less than 80% at 10 μg mL^{-1}. Then FCM results indicated a concentration-dependent increase in the apoptosis rate, and the apoptosis ratio of LLC cells treated with Tf–MnS reached 39.93%. Next, ROS detection results showed that LLC cells exhibited a higher green fluorescence intensity as the concentration increased, suggesting that Mn^{2+} catalyzed a Fenton-like reaction, leading to the generation of more $^{\bullet}OH$ to induce tumor cell death (Fig. 2G and H). These results confirm that Tf–MnS effectively inhibits tumor cell proliferation while maintaining favorable biocompatibility with normal cells.

2.3 Mechanism of the self-enhanced therapy of Tf–MnS

In the following experiments, the mechanism of Tf–MnS in tumor treatment was investigated. Tf–MnS effectively decomposes in an acidic environment, resulting in tumor cell death through the promotion of LPO and induction of ferroptosis, as depicted in Fig. 3A. H_2S gas exerts a specific inhibitory effect on the CAT activity of tumor cells, decreasing H_2O_2 consumption and enhancing the generation of intracellular ROS.[20] Therefore, the H_2S level in LLC cells post Tf–MnS treatment was explored. The results showed that LLC cells with Tf–MnS treatment exhibited a dose-dependent increase in green fluorescence, possibly due to the tumor acidic environment causing the pH-responsive Tf–MnS nanoplatform to decompose into Mn^{2+} and H_2S (Fig. 3B and Fig. S6, ESI†). Subsequent verification of
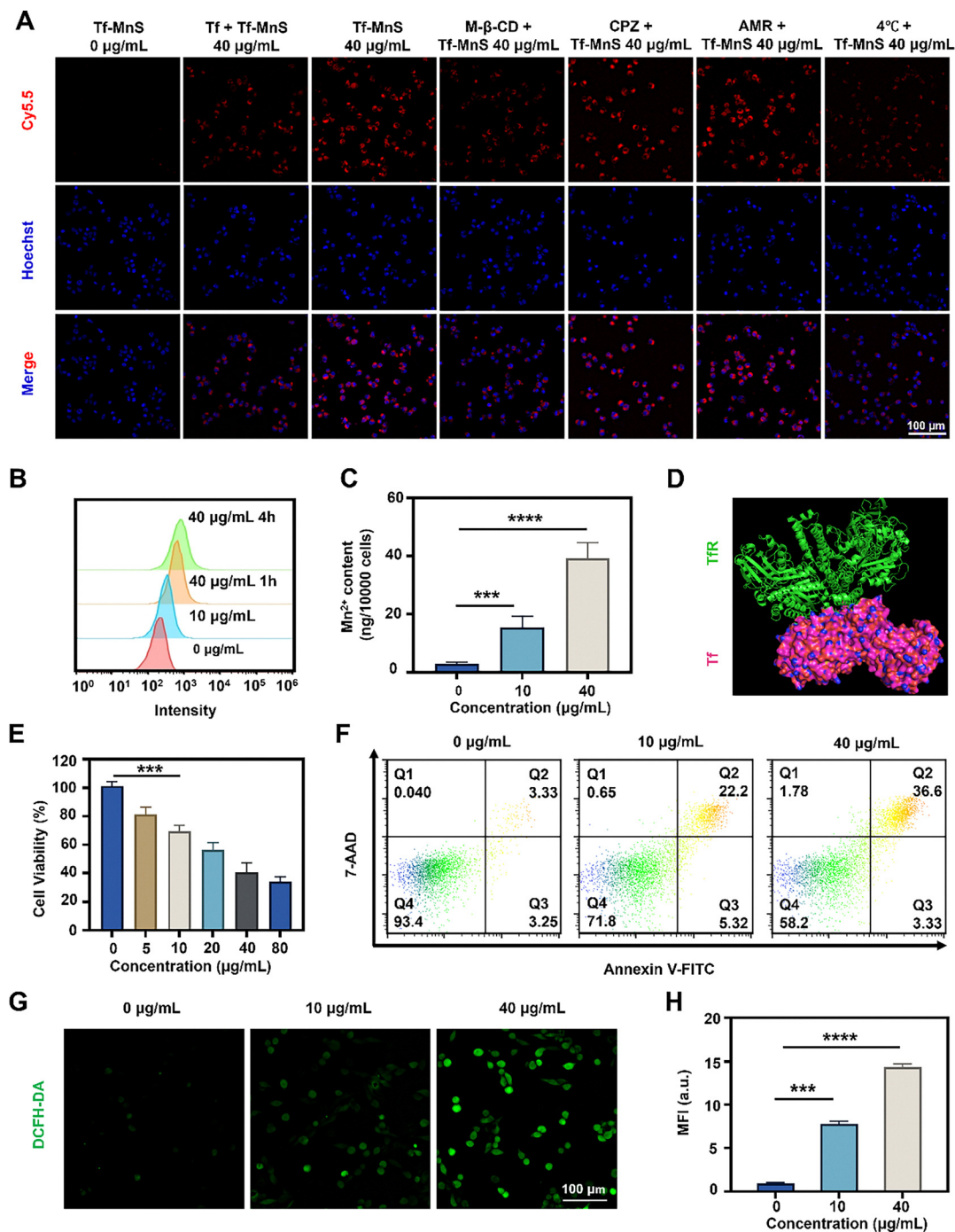
Fig. 2 (A) CLSM observation of the cellular uptake of Tf−MnS following various treatments. (B) FCM analysis for dosage- and time-dependent uptake. (C) ICP-OES analysis of intracellular Mn^{2+} uptake by LLC cells following Tf−MnS treatment. (D) Molecular docking validated the strong binding affinity between Tf (6wb6) and TfRs (1cx8). (E) Cell viability of LLC cells treated with Tf−MnS. (F) FCM analysis of apoptosis in LLC cells following various treatments. (G) Levels of reactive ROS in LLC cells following various treatments and (H) the corresponding statistical data ($n = 3$, $**p < 0.01$, $***p < 0.001$, and $****p < 0.001$).

CAT activity indicated a decline, possibly due to the effective inhibition of CAT activity by the generated H_2S gas (Fig. 3C). This could address the issue of the inadequate H_2O_2 content in CDT within the intratumoral region to some extent. In summary, diverse experimental data demonstrate that Tf−MnS can not only induce tumor cell death through $^\bullet OH$ produced by the

Fenton-like reaction of Mn^{2+}, but also suppress CAT activity by generating H_2S gas. This process effectively promotes more ROS generation, thereby enhancing the therapeutic efficacy against tumors.

MnS decomposes in acidic environments, and $^\bullet OH$ can interact with molecules like lipids, DNA, and proteins within
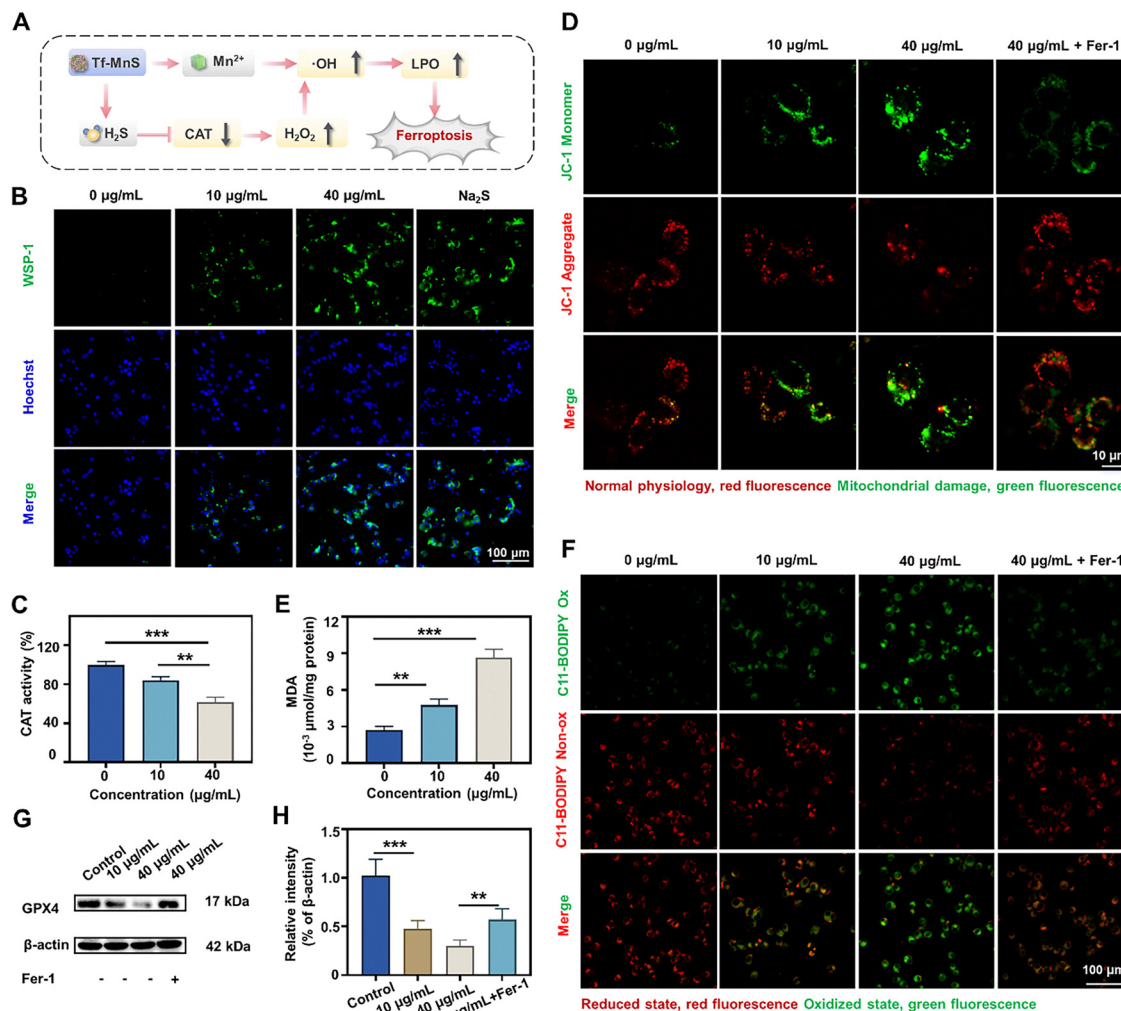
Fig. 3 (A) Schematic representation of the mechanism by which Tf–MnS is utilized for tumor therapy. (B) CLSM observation of the H₂S production in LLC cells after various treatments. (C) CAT inhibitory activity of Tf–MnS. (D) CLSM observations of LLC cells stained with the JC-1 probe following various treatments. (E) MDA detection in LLC cells treated with Tf–MnS. (F) Detection of intracellular LPO using the C11-BODIPY 581/591 probe. (G) Western blots of GPX4 with various treatments and (H) the corresponding statistical data ($n = 3$, $**p < 0.01$, and $***p < 0.001$).

mitochondria, causing mitochondrial lipid peroxidation, electron transport chain damage, and alterations in mitochondrial membrane potential.[13] By utilizing the JC-1 probe to assess mitochondrial function, the outcomes indicated when exposed to high concentration of Tf–MnS nanoplatform, the green fluorescence representing the JC-1 monomer brilliantly enhanced, while the red fluorescence representing the JC-1 aggregate descended gradually, but at the same concentration, the addition of ferroptosis inhibitors (Fer-1) can effectively reduce green fluorescence (Fig. 3D and Fig. S7, ESI†). The transition of JC-1 from an aggregated to a dispersed state was linked to the decline in the mitochondrial membrane potential and the mitochondrial damage induced by Tf–MnS. Subsequently, a malondialdehyde (MDA) kit and C11-bodipy 581/591 probe were utilized to assess the level of LPO in the cells. The results showed that both the intracellular MDA level and LPO level escalated with an increase in concentration, but the LPO levels of the groups with Fer-1 decreased compared with

those without when comparing the same concentration (Fig. 3E, F and Fig. S8, ESI†). This escalation was attributed to the ability of the high concentration of Tf–MnS to enhance oxidative stress in cells, consequently elevating the level of LPO. The substantial accumulation of LPO resulted in the subsequent induction of cell ferroptosis, a process further supported by the decreased expression of recombinant glutathione peroxidase 4 (GPX4) (Fig. 3G and H). These outcomes serve as compelling evidence that Tf–MnS effectively triggers ferroptosis in tumor cells.

2.4 MRI performance of Tf–MnS in vitro and the imaging effect of subcutaneous tumors and pulmonary nodules

The T_1-weighted MR effect of the Tf–MnS nanoplatform was validated through both in vivo and in vitro experiments. Firstly, the longitudinal relaxation (r_1) of Tf–MnS was determined to be 3.3581 mM⁻¹ s⁻¹ and 7.5253 mM⁻¹ s⁻¹ at pH 7.4 and pH 5.5, respectively, which were notably higher than that of Gd-DTPA

(3.2915 mM^{-1} s^{-1}) under acidic conditions (Fig. 4A and B). Additionally, the T_1-weighted MR images of the agarose gel containing Tf–MnS exhibited a dose-dependent enhancement of MR contrast at both pH 7.4 and pH 5.5 (Fig. 4C) and the image is more obvious under acidic conditions, with significantly brighter images compared to those obtained with Gd-DTPA (Fig. S9, ESI†). The elevated r_1 value of the Tf–MnS establishes a crucial foundation for further investigations into its MRI performance *in vivo*. Subsequently, the *in vivo* nuclear magnetic properties of the nanoprobe were investigated using a 9.4T MR scanner. Following the administration of Tf–MnS and Gd-DTPA *via* tail vein injection, MR imaging of LLC tumor-bearing mice was conducted at 0, 30, 60, 90, and 120 min. Remarkably, mice treated with Tf–MnS exhibited significant

T_1-weighted signal enhancement in the tumor region post-injection, with the tumor signals peaking at 60 min and relative signal-to-noise ratios (ΔSNR) of 46.33% (coronal) and 43.67% (axial). Subsequently, the signal gradually decreased but remained notably higher than the maximum ΔSNR observed in the Gd-DTPA control group at 30 min, which was 24.67% (coronal) and 24.33% (axial) (Fig. 4D–H). Moreover, even at the 120 min mark, the ΔSNR of the Tf–MnS group surpassed that of the Gd-DTPA group, indicating the superior MR contrast enhancement effect by the enhanced permeability and retention effect of Tf–MnS. Next, a lung metastatic model was established and MRI was performed. It was found through comparison that Tf–MnS had a better imaging effect at 30 min than Gd-DTPA. The image of the pulmonary metastatic lesion
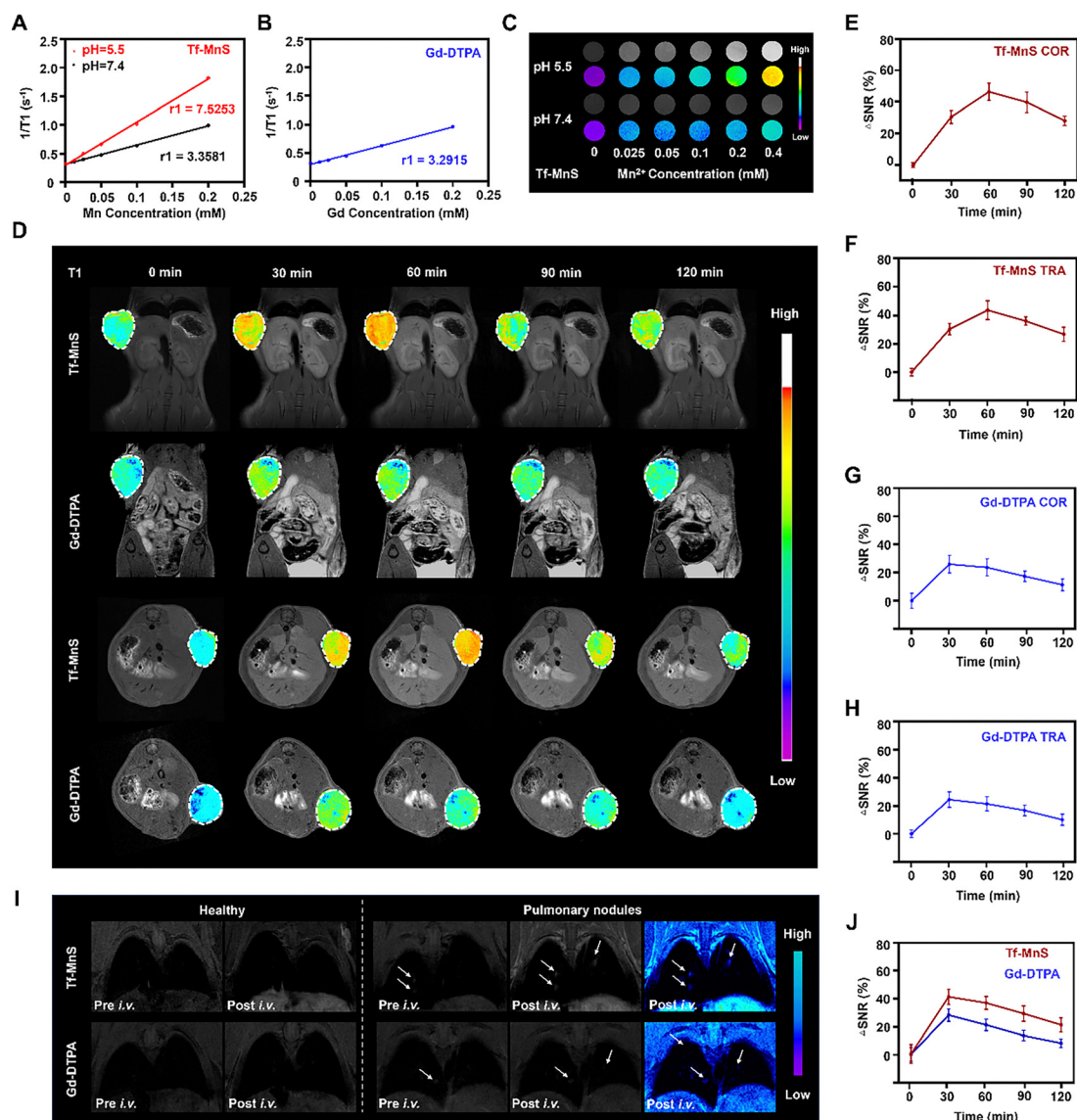

Fig. 4 (A) and (B) The longitudinal relaxation rates (r_1) of Tf–MnS and Gd-DTPA. (C) T_1-weighted MR images of agarose gels containing Tf–MnS at pH 7.4 and pH 5.5. (D) Coronal and axial T_1-weighted MR images acquired at various time points after injection of Tf–MnS and Gd-DTPA. (E)–(H) Comparative analysis of the change in ΔSNR in coronal and axial tumor MRI images. (I) Coronal T_1-weighted MR images acquired before and 30 min after the injection of Tf–MnS and Gd-DTPA in the pulmonary metastatic lesion model and (J) analysis of the ΔSNR change at various time points.
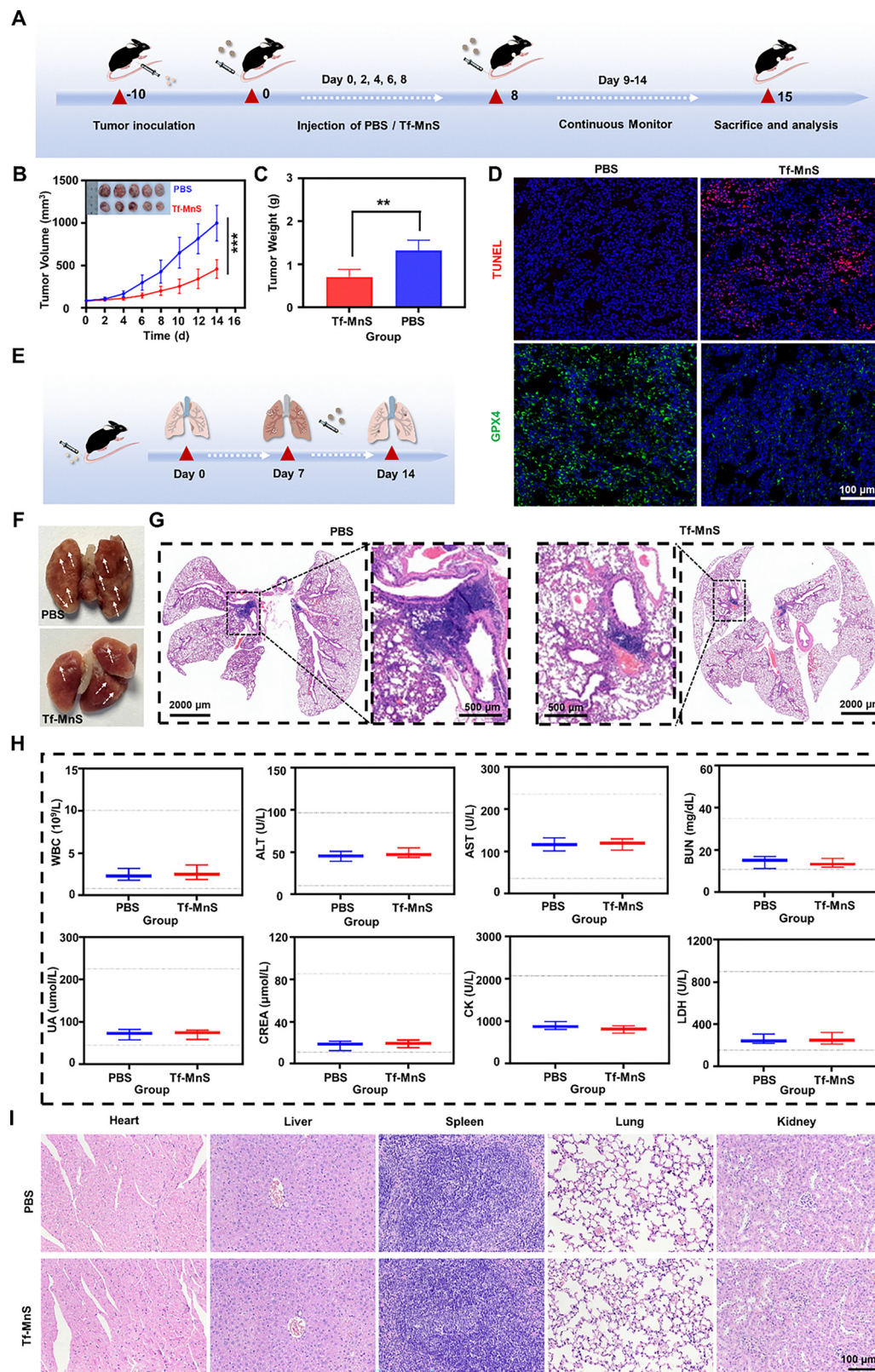
Fig. 5 (A) Flowchart outlining the processing plan for the *in vivo* experimental design. (B) The tumor growth curves and the photographic representation of tumor tissue from LLC tumor-bearing mice. (C) Comparative tumor weights of mice treated with PBS and Tf−MnS. (D) TUNEL and GPX4 staining for tumor tissues with PBS/Tf−MnS treatments. (E) Schematic diagram of the establishment of the pulmonary metastatic model and the treatment process. (F) Representative images of the pulmonary metastatic lesions on lung tissue. (G) H&E staining of the pulmonary metastatic lesions after various treatments. (H) The blood routine and blood biochemical indicators of mice after Tf−MnS treatments. (I) H&E staining of major organs harvested from mice (n = 5, **p < 0.01, and ***p < 0.001).

was clearer, and the ΔSNR reached 40.33%, which was 1.42 times that of Gd-DTPA (Fig. 4I and J). Concurrently, T_1-weighted MRI signals in the liver and kidney regions demonstrated a similar enhancement following the intravenous administration of Tf–MnS, indicating its potential effective metabolism (Fig. S10, ESI†). These findings offer a reliable basis for the precise localization of tumors and pulmonary metastatic lesions, underscoring the effectiveness of Tf–MnS in this regard.

2.5 *In vivo* therapeutic efficacy and biosafety of Tf–MnS

In prior *in vitro* experiments, the Tf–MnS nanoplatform exhibited an excellent anti-tumor effect, necessitating further validation of its therapeutic efficacy in tumor-bearing mice with LLC cells. Once the tumor volume reached approximately 80 mm³, the mice were randomly divided into two groups, the PBS group and the Tf–MnS group. Over the subsequent two weeks, Tf–MnS was administered every two days, totaling five injections, with tumor sizes and mouse weights monitored every other day (Fig. 5A). On day 14, the mice were euthanized to weigh tumors and conduct photography, which revealed that the tumor volume in the PBS group was significantly larger than that in the Tf–MnS group, and the results showed rapid tumor growth in the PBS control group, with an increase from 81.89 mm³ to 997.95 mm³ within 2 weeks. In contrast, mice treated with Tf–MnS demonstrated significant tumor suppression, with tumor sizes ranging from 78.37 mm³ to 456.45 mm³, which were significantly smaller than those of the control group (Fig. 5B), as evidenced by the comparison of tumor weights after dissection (Fig. 5C). The terminal deoxynucleotidyl transferase-mediated dUTP nick end labeling (TUNEL) assay also confirmed increased damage in tumor cells in the Tf–MnS group, and the reduction of green fluorescence in GPX4 immunofluorescence staining images further proves that Tf–MnS can effectively promote ferroptosis in tumor tissues (Fig. 5D). These findings further substantiate the therapeutic potential of Tf–MnS in inhibiting tumor growth in mice. Subsequently, we injected LLC cells into mice through the tail vein to establish a pulmonary metastatic lesion model and performed Tf–MnS treatment 7 days later (Fig. 5E). After the treatment, anatomy examination and hematoxylin and eosin (H&E) staining of the lungs were performed. As shown in the typical image of lung tissue (Fig. 5F), the PBS group showed a higher number of lung metastatic lesions and a rougher lung surface, while the Tf–MnS group displayed a limited number of lung metastatic lesions with smoother surfaces (Fig. S11, ESI†). Additionally, the Tf–MnS group had a smaller lung weight in the dissected lung tissue than the PBS group (Fig. S12, ESI†), indicating that the lung metastasis range was reduced and inflammation was alleviated. Furthermore, H&E staining results of lung tissue showed that in the lung tissue of the PBS group, more deeply stained areas of the nucleus could be seen, with more tumor cell infiltration and inflammatory responses than in the Tf–MnS group (Fig. 5G). This indicated that pulmonary metastasis has been suppressed to a certain extent.

Concurrently, the ideal tumor treatment strategy should not only achieve an effective therapeutic effect but also ensure good biological safety with minimal damage to the whole body. Comparison of the weights of the mice in two groups revealed no significant changes (Fig. S13, ESI†). Subsequent analyses of blood samples from mice injected with Tf–MnS demonstrated that all indices of liver and kidney function remained within the normal range (Fig. 5H). Furthermore, the hemolysis rates for different concentrations of Tf–MnS across the groups remained below 5% (Fig. S14, ESI†). Additionally, representative H&E staining images indicated the absence of obvious tissue pathological changes and inflammatory reactions in the main organs of mice (Fig. 5I). This implies that the nanoplatform does not exert adverse effects on the organs or metabolism of mice. Overall, Tf–MnS exhibits favorable biocompatibility *in vivo* and is not associated with systemic toxicity.

3. Conclusions

In conclusion, this study has developed a new nanoplatform for integrated MRI-guided diagnosis and treatment. Initially, the r_1 relaxation rate of the Tf–MnS nanoplatform significantly increases in an acidic environment, and the T_1 imaging effect is superior to that of the commonly used Gd-based contrast agents in clinical practice. This is helpful for enhancing MR imaging of tumors and pulmonary metastatic lesions and for early and precise diagnosis. Concurrently, Tf prompts the nanoplatform to efficiently target the sites of tumors and pulmonary metastatic lesions, and then Mn^{2+} and H_2S are released in the slightly acidic tumor environment due to pH-responsive decomposition, potentiating self-enhanced ROSs in tumor cells, which can further inhibit cancer progression by effectively inducing ferroptosis. Most importantly, the Tf–MnS nanoplatform demonstrates excellent biocompatibility and is devoid of significant toxicity and side effects. Therefore, the Tf–MnS nanoplatform represents a promising new avenue for integrated MRI-guided tumor diagnosis and therapy.

4. Materials and methods

4.1 Materials

Tf was purchased from Shanghai Yuanye Bio-Technology. Manganese chloride tetrahydrate ($MnCl_2 \cdot 4H_2O$) and sodium sulfide nonahydrate ($Na_2S \cdot 9H_2O$) were obtained from Aladdin (Shanghai, China). Phosphate-buffered saline (PBS), fetal bovine serum (FBS), and high-glucose Dulbecco's modified Eagle's medium (DMEM) were obtained from Gibco (Carlsbad, CA). MTT was bought from Sangon Biotech (Shanghai, China). WSP-1 was purchased from Shanghai Maokang Biotechnology Co., Ltd. A mitochondrial membrane potential assay kit with JC-1 and a catalase (CAT) activity assay kit were purchased from Solarbio Science & Technology Co., Ltd (Beijing, China). BODIPY581/591-C11 was purchased from Thermo Fisher Scientific Co. (Maryland, USA).

4.2 Animals and tumor model

C57BL/6 mice (6 weeks) were obtained from Jinan Xingkang Biotechnology Co., Ltd (Jinan, China). All animal procedures

were performed in accordance with the Guidelines for Care and Use of Laboratory Animals of Shandong Cancer Hospital and Institute, Shandong First Medical University and approved by the Animal Ethics Committee of China (2023003137).

4.3 Synthesis of Tf–MnS

Initially, 2 mg of Tf was dissolved in 6 mL of Na_2S solution (6 mM), followed by pH value adjustment to $\sim$7.6 using dilute HCl/NaOH solutions under continuous magnetic stirring. Subsequently, 2 mL of $MnCl_2$ solution (10 mM) was introduced dropwise into the mixture. The reaction system was maintained in an ice-water bath under nitrogen atmosphere protection to prevent oxidation, with vigorous stirring sustained for 4 h to ensure complete nanoparticle formation. Then, the resulting mixture was subjected to ultrafiltration centrifugation at 3800g for 10 min. After initial concentration, 10 mL of deionized water was added and ultrafiltration purification was carried out under the same conditions. This step was repeated three times to remove unreacted precursors.

4.4 Characterization of Tf–MnS

The morphology of Tf–MnS was obtained using a 120 KV TEM (HT7800). The phase and crystal structure of the Tf–MnS nanoplatforms were determined using XRD (MAX-2600, Rigaku D, Japan). The elemental composition on the surface of the nanoplatform and the chemical states of elements were measured using XPS (K-Alpha, Thermo Scientific, USA). The zeta potential was detected using a DLS detector (NanoBrook 90Plus PALS, Brookhaven, USA).

4.5 Mn^{2+} detection

Tf–MnS (1 mg mL^{-1}) was dispersed in buffer solutions of varying pH values (pH 5.5 and pH 7.4) and incubated at room temperature for 24 h. At predetermined time intervals, the mixtures were centrifuged to collect the supernatant, and the Mn^{2+} content in the supernatant was quantified by ICP-OES.

4.6 H_2S detection

Tf–MnS (1 mg mL^{-1}) was dispersed in PBS with varying pH values (pH 5.5 and pH 7.4), followed by incubation at room temperature for 2 h. The mixture was centrifuged to collect the supernatant, into which $AgNO_3$ (1 mg mL^{-1}) was added and thoroughly mixed. The resulting solution was then incubated at room temperature for an additional 12 h.

4.7 Biocompatibility and cytotoxicity assay

MLE-12, HUVEC and LLC cells were inoculated in 96-well plates (1 $\times$ 10^4 cells per well) and cultured for 24 h. Then, LLC cells were treated with Tf–MnS at different concentrations for 24 h. The cell survival rate was tested by the MTT method.

4.8 Cell uptake

4.8.1 CLSM. LLC cells were inoculated in confocal dishes (1.5 $\times$ 10^5 cells per dish) and cultured for 24 h. The next day, Tf–MnS and Cy5.5 were stirred in the dark for 20 min in advance, and then LLC cells were treated with Tf–MnS-Cy5.5

for 4 h, and stained with Hoechst33342 for 20 min. Finally, the cells were washed twice and the images were obtained using a fluorescence microscope.

4.8.2 FCM investigation. LLC cells were inoculated in 6-well plates (2 $\times$ 10^5 cells per well), and then treated with Tf–MnS-FITC for 4 h. Then, the samples were subjected to FCM testing.

4.8.3 ICP-OES. LLC cells were taken and inoculated in 6-well plates (2 $\times$ 10^5 cells per well). The next day, the LLC cells were treated with Tf–MnS for 6 h and completely washed to remove the nanoprobe. Subsequently, the LLC cells were nitrated with aqua regia and tested by ICP-OES.

4.9 Molecular docking of Tf and TfR

The corresponding protein ID was retrieved from the UniProt database, and a suitable protein structure was downloaded from the Protein Data Bank (PDB). The ligand structure was subsequently obtained from the PubChem database. Putative ligand-binding regions on the target molecule were identified and annotated using PyMOL. Finally, molecular docking was performed with AlphaFold3 to predict interaction modes.

4.10 Intracellular $^{\bullet}OH$ detection

LLC cells were inoculated in confocal dishes (2 $\times$ 10^5 cells per dish) and incubated for 24 h. Subsequently, the cells were treated with different concentrations of Tf–MnS for 4 h. Then, the cells were incubated with 2,7-dichlorodihydrofluorescein diacetate (H2DCFDA) in the dark for 20 min. Intracellular fluorescence was observed by CLSM to investigate ROS production.

4.11 Intracellular H_2S detection

LLC cells were inoculated in a confocal dish (2 $\times$ 10^5 cells per dish) and cultured for 24 h, and then different concentrations of Tf–MnS and the positive control Na_2S were added, respectively, for treatment for 5 h. The cells were incubated with H_2S detection probes according to the instructions, and the level of H_2S in the cells was observed by CLSM.

4.12 Evaluation of CAT activity

LLC cells were inoculated in 6-well plates (2 $\times$ 10^5 cells per well) and cultured for 24 h. Then, the cells were treated with Tf–MnS, and after 12 h, the cells were treated with a catalase assay kit according to the instructions. Next, relevant indicators were detected and calculated.

4.13 Evaluation of LPO and the mitochondrial membrane potential

LLC cells were inoculated in a confocal dish (1.5 $\times$ 10^5 cells per dish) and cultured for 24 h. Then, the cells were treated with different concentrations of Tf–MnS, and after 5 h the cells were stained with C11-BODIPY 581/591 and a JC-1 assay kit according to the instructions, and LPO and the mitochondrial membrane potential were determined by CLSM.

4.14 Evaluation of MDA

LLC cells were taken and inoculated in 6-well plates (2×10^5 cells per well). After 12 h, the level of MDA in the cells was tested using an MDA assay kit according to the instruction manual for the reagent kit.

4.15 Western blot

Samples were separated via SDS-PAGE, transferred onto nitrocellulose membranes, blocked with non-fat milk, and probed with anti-GPX4 and anti-β-actin primary antibodies, followed by secondary antibodies. Chemiluminescence signals were captured in the end.

4.16 MRI study

Tf–MnS and Gd-DTPA were intravenously injected through the tail vein (Mn^{2+}/Gd^{3+} 0.04 mmol kg^{-1}), and T_1-weighted images of the mice were acquired using a 9.4 T animal MRI scanner. The gradient system allowed for a maximal gradient strength of 660 mT m^{-1} with a slew rate of 4570 T m^{-1} s^{-1}. The outer and inner diameters were 75 mm and 40 mm, respectively. A set of scout images were obtained in the coronal view and the axial views of the tumor before scanning. The T_1-weighted imaging parameters were as follows: TE = 6 ms, TR = 800 ms, excitation angle = 90°, field of view = 4.0×3.0 cm^2, matrix size = 256×256, slice thickness = 0.7 mm, and the number of repetitions per slice = 20.

4.17 In vivo tumor and pulmonary metastatic lesion inhibition study

LLC cells were suspended in serum-free medium (1×10^7 cells per mL) and 100 μL were injected subcutaneously to establish a hormonal C57BL/6 mouse model. The measurements of mice body weights and tumor volumes were recorded using a balance and digital caliper every other day during the entire treatment period. The weights of the tumors in the mice from different groups were also measured at the end of the treatments. To establish the pulmonary metastatic lesion model in C57BL/6 mice, 2.5×10^5 LLC cells in 120 μL of PBS were injected into every mouse through the tail vein. Seven days post-injection, treatment commenced with Tf–MnS (Mn^{2+}, 2 mg kg^{-1}) administered via tail vein injection every two days, for a total of three treatments.

4.18 Bio-safety assessment

4.18.1 Hemolysis test. Fresh blood was collected from mice and washed with PBS to obtain red blood cells (RBCs). The Tf–MnS was added to the RBC suspension at different concentrations. One tube of RBCs was diluted with PBS as the negative control, and another RBCs was diluted with ultrapure water as a positive control. All the samples were incubated at 37 °C for 5 h, and the hemolysis rate was tested and analyzed.

4.18.2 H&E staining. The mice were sacrificed after PBS/Tf–MnS treatment, and the main organs were dissected. H&E staining of major organs was applied to detect the condition of tissues.

Author contributions

Liya Tian and Pengju Ma performed subject conceptualization, experimental methodology, result validation, formal analysis and writing manuscripts. Shunzhen Zheng and Xiao Sun performed conceptualization, supervision and financial support. Wenxiu Zhuang, Yinlong Xu, Lihua Pang, Kai Guo, Ke Ren and Xueli Xu performed methodology and manuscript review. All the authors read, revised and reviewed the final manuscript.

Conflicts of interest

There are no conflicts to declare.

Data availability

The data supporting this article have been included as part of the ESI.†

Acknowledgements

References

1 Q. Tao, G. He, S. Ye, D. Zhang, Z. Zhang, L. Qi and R. Liu, *J. Nanobiotechnol.*, 2022, **20**, 18.

2 T. Anani, S. Rahmati, N. Sultana and A. E. David, *Theranostics*, 2021, **11**, 579–601.

3 D. Lau, P. G. Corrie and F. A. Gallagher, *J. ImmunoTher. Cancer*, 2022, **10**, e004708.

4 S. P. Rowe and M. G. Pomper, *Ca-Cancer J. Clin.*, 2022, **72**, 333–352.

5 H. Li and T. J. Meade, *J. Am. Chem. Soc.*, 2019, **141**, 17025–17041.

6 C.-T. Yang, A. Hattiholi, S. T. Selvan, S. X. Yan, W.-W. Fang, P. Chandrasekharan, P. Koteswaraiah, C. J. Herold, B. Gulyás, S. E. Aw, T. He, D. C. E. Ng and P. Padmanabhan, *Acta Biomater.*, 2020, **110**, 15–36.

7 D. Ndiaye, P. Cieslik, H. Wadepohl, A. Pallier, S. Même, P. Comba and É. Tóth, *J. Am. Chem. Soc.*, 2022, **144**, 22212–22220.

8 F. Carniato, M. Ricci, L. Tei, F. Garello, C. Furlan, E. Terreno, E. Ravera, G. Parigi, C. Luchinat and M. Botta, *Small*, 2023, **19**, 2302868.

9 G. Ma, X. Zhang, K. Zhao, S. Zhang, K. Ren, M. Mu, C. Wang, X. Wang, H. Liu, J. Dong and X. Sun, *ACS Nano*, 2024, **18**, 3369–3381.

10 H. Lu, A. Chen, X. Zhang, Z. Wei, R. Cao, Y. Zhu, J. Lu, Z. Wang and L. Tian, *Nat. Commun.*, 2022, **13**, 7948.

11 C. Xie, D. Cen, Z. Ren, Y. Wang, Y. Wu, X. Li, G. Han and X. Cai, *Adv. Sci.*, 2020, **7**, 1903512.

12 S. Liu, L. Tian, M. Mu, Z. Liu, M. Dong, Y. Gong, H. Liu, X. Wang, Q. Meng, H. Zhang and X. Sun, *Adv. Healthcare Mater.*, 2024, **13**, 2303939.

13 Y. Gong, K. Guo, S. Cai, K. Ren, L. Tian, Y. Wang, M. Mu, Q. Meng, J. Liu and X. Sun, *Biomater. Res.*, 2024, **28**, 0116.

14 J. Cui, G. Wang, L. X. Yip, M. Dong, M. Mu, L. Tian, Y. Gao, Q. Fan, Q. Zhu, X. Zhao, X. Xu, D. T. Leong and X. Sun, *Adv. Funct. Mater.*, 2024, **34**, 2410748.

15 K. Guo, H. Liu, M. Zhang, N. Ni, M. Mu, K. Ren, J. Chen, Q. Fan, X. Xu, X. Sun and X. Wang, *Chem. Eng. J.*, 2025, **504**, 158754.

16 S. Bai, Z. Lu, Y. Jiang, X. Shi, D. Xu, Y. Shi, G. Lin, C. Liu, Y. Zhang and G. Liu, *ACS Nano*, 2022, **16**, 997–1012.

17 S. Zhang, X. Wu, X. Liao and S. Zhang, *J. Am. Chem. Soc.*, 2024, **146**, 8567–8575.

18 J.-J. Zou, G. Wei, C. Xiong, Y. Yu, S. Li, L. Hu, S. Ma and J. Tian, *Sci. Adv.*, 2022, **8**, eabm4677.

19 S. Wu, Y. Ye, Q. Zhang, Q. Kang, Z. Xu, S. Ren, F. Lin, Y. Duan, H. Xu, Z. Hu, S. Yang, H. Zhu, M. Zou and Z. Wang, *Adv. Sci.*, 2023, **10**, 2203742.

20 Y. Gao, M. Mu, Y. Wei, B. Yan, H. Liu, K. Guo, M. Zhang, X. Dai, X. Sun and D. T. Leong, *Bioact. Mater.*, 2025, **43**, 564–578.